TECHNICAL REPORT
https://doi.org/10.1038/s41593-018-0091-7

nature neuroscience

Nontoxic, double-deletion-mutant rabies viral vectors for retrograde targeting of projection neurons

Soumya Chatterjee[1], Heather A. Sullivan[2], Bryan J. MacLennan[1], Ran Xu[2], YuanYuan Hou[2], Thomas K. Lavin[2], Nicholas E. Lea[2], Jacob E. Michalski[2], Kelsey R. Babcock[2], Stephan Dietrich[2], Gillian A. Matthews[3,4], Anna Beyeler[3,4], Gwendolyn G. Calhoon[3,4], Gordon Glober[3,4], Jennifer D. Whitesell[1], Shenqin Yao[1], Ali Cetin[1], Julie A. Harris[1], Hongkui Zeng[1], Kay M. Tye[3,4], R. Clay Reid[1] and Ian R. Wickersham[2*]

Recombinant rabies viral vectors have proven useful for applications including retrograde targeting of projection neurons and monosynaptic tracing, but their cytotoxicity has limited their use to short-term experiments. Here we introduce a new class of double-deletion-mutant rabies viral vectors that left transduced cells alive and healthy indefinitely. Deletion of the viral polymerase gene abolished cytotoxicity and reduced transgene expression to trace levels but left vectors still able to retrogradely infect projection neurons and express recombinases, allowing downstream expression of other transgene products such as fluorophores and calcium indicators. The morphology of retrogradely targeted cells appeared unperturbed at 1 year postinjection. Whole-cell patch-clamp recordings showed no physiological abnormalities at 8 weeks. Longitudinal two-photon structural and functional imaging in vivo, tracking thousands of individual neurons for up to 4 months, showed that transduced neurons did not die but retained stable visual response properties even at the longest time points imaged.

Since their introduction to neuroscience in 2007[1], recombinant rabies viral vectors have come to occupy a unique role in the field. Their most important and widespread use is in monosynaptic tracing, which allows identification and study of neurons directly presynaptic to single neurons or targeted cell types[2–12]. Another important application is retrograde infection of projection neurons, to express transgene products such as fluorophores[1,9,13], opsins[14–19] or activity indicators[20–22] selectively within groups of neurons targeted on the basis of their axonal projections. Both of these applications have yielded insights into the organization of neural circuits in a wide variety of regions, ranging from cerebral cortex to spinal cord.

These vectors, however, come with the major downside of causing nontrivial cytotoxicity. All rabies viral (RV) vectors used to date for retrograde targeting and monosynaptic tracing (which we refer to below as 'first-generation' or 'ΔG' rabies viral vectors) have a single gene, *G* (NCBI symbol: *RABVgp4*), encoding the viral envelope glycoprotein, deleted from their genomes, with the other four viral genes left intact[1] (Fig. 1a). Because the glycoprotein is only required for the final steps of the viral life cycle, this deletion prevents the virus from spreading beyond initially infected cells, but it does not prevent the virus from completing the entirety of its replication cycle up to that point. This is a double-edged sword. On the one hand, it results in rapid and high-level expression of transgenes, which can be extremely useful for such applications as imaging fine cellular processes or optogenetically manipulating neuronal activity[1,14,15,18,23]. On the other hand, it also results in fairly rapid cytotoxicity, with death of many or most infected cells occurring on a timescale of ~2 weeks[1]. This, of course, prevents the vectors from being used for long-term imaging or optogenetic experiments.

Efforts to reduce the toxicity of RV vectors have been made previously. It has recently been reported, for example, that first-generation RV vectors from a different parent strain (CVS N2c, rather than SAD B19) allow infected neurons to survive longer[24]. However, to our knowledge no claim has been made, and no evidence suggests, that the use of CVS N2c or any other strain completely eliminates the toxicity of first-generation vectors. It has also recently been reported that addition of a proteasome-targeting destabilization domain to the viral nucleoprotein removes viral toxicity[25]. However, because individual infected neurons were not tracked over time in these studies, it is difficult to assess whether cytotoxicity was completely abolished.

Here we take a quite different approach toward eliminating toxicity (Fig. 1b). We introduce a new class of RV vector, from the genome of which we have deleted a second and arguably much more fundamental gene. Known as *L* (for 'large protein' gene (NCBI symbol: *RABVgp5*), *P* being already taken as the name of the viral phosphoprotein gene), this second deleted gene encodes the viral polymerase, which is required both for transcription of viral genes and for replication of the viral genome[26]. We hypothesized that deletion of the polymerase gene would reduce expression of viral genes and transgenes to miniscule levels, resulting in a vector that would cause no detectable cytotoxicity whatsoever. We further hypothesized that, if such vectors encoded recombinases, the tiny remnant transcription levels (resulting from the activity of the few starter copies of the polymerase that are packaged in each viral particle[27])

[1]Allen Institute for Brain Science, Seattle, WA, USA. [2]McGovern Institute for Brain Research, Massachusetts Institute of Technology, Cambridge, MA, USA. [3]Picower Institute for Learning and Memory, Massachusetts Institute of Technology, Cambridge, MA, USA. [4]Department of Brain and Cognitive Sciences, Massachusetts Institute of Technology, Cambridge, MA, USA. *e-mail: wickersham@mit.edu

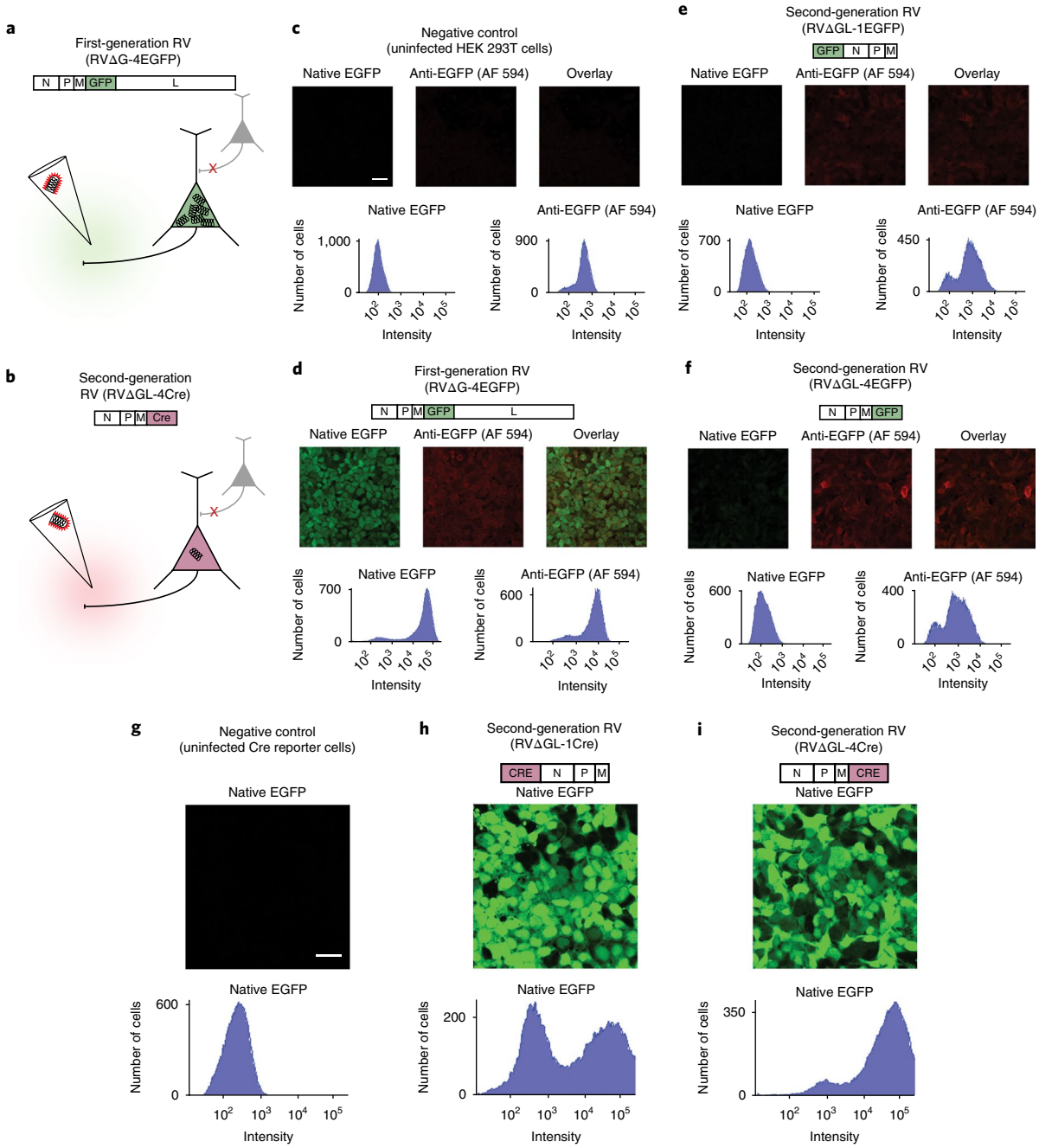

Fig. 1 | Deletion of the RV polymerase gene reduces gene expression to trace levels but leaves recombinase-encoding vectors still able to cause reporter expression in cell culture. a,**b**, Strategy for eliminating the toxicity of rabies viral vectors. (**a**) In first-generation vectors, only the *G* gene, encoding the envelope glycoprotein, is deleted. This prevents the virus from spreading beyond directly infected cells but still allows the virus to replicate within them, resulting in rapid, high transgene expression as well as severe toxicity on a timescale of 1–2 weeks. (**b**) In the second-generation RV vectors introduced here, the *L* gene, encoding the viral polymerase, has also been deleted to reduce expression from the viral genome to trace levels. Because transgene expression should therefore also be reduced, the gene for a recombinase, such as Cre or Flp, is used to allow the expected very low expression levels to cause subsequent expression of a reporter at experimentally useful levels. **c**–**i**, Results in cell culture: images and flow-cytometric histograms show EGFP fluorescence in cells infected by first- and second-generation RV vectors. Left images and histograms in **c**–**f** show native EGFP fluorescence; middle images and right histograms in **c**–**f** show anti-GFP immunolabeling with Alexa Fluor-594 (AF 594) secondary antibody; right images show overlay of left and middle images. *X* axes of histograms are log scale with arbitrary units. (**c**) Negative control: HEK 293T cells not infected with any virus do not express EGFP, as indicated by the single peak at a very low fluorescence level. (**d**) A first-generation RV vector encoding EGFP causes infected HEK 293T cells to fluoresce brightly, as shown by the peak far to the right of the histogram (the leftmost peak represents uninfected cells in the same well). (**e**,**f**) Second-generation RV vectors encoding EGFP cause almost undetectable EGFP expression in infected cells, as shown by histograms that resemble those of the uninfected cells shown in **c**; immunostaining for EGFP shows that virus is nonetheless present and producing EGFP at low levels. This is true whether the EGFP gene is placed in the most highly expressing locus at the start of the viral genome (**e**) or in the 'usual' transgene locus of the deleted *G* gene (**f**). (**g**–**i**) We then constructed second-generation RV vectors encoding Cre recombinase and tested them in reporter cells that express EGFP when Cre is expressed. (**g**) Negative control: uninfected reporter cells express very little EGFP. (**h**,**i**) Reporter cells infected with second-generation RV vectors encoding Cre express abundant EGFP. This is true whether the *Cre* gene is inserted at the start of the RV genome (**h**) or into the *G* locus (**i**). Experiments in this figure were performed twice with similar results each time. Scale bars, 33 μm.

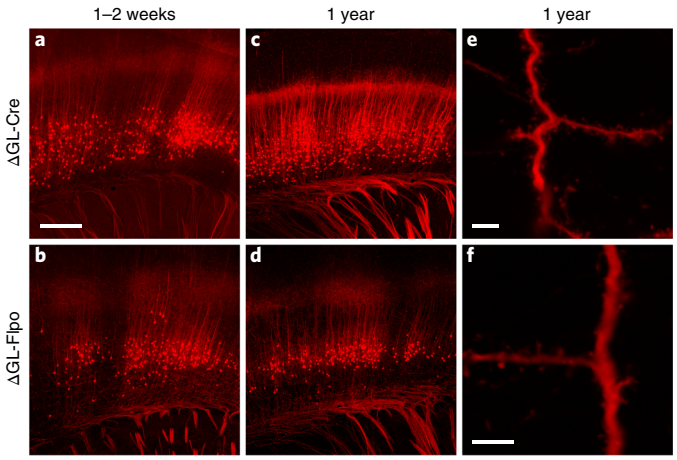

Fig. 2 | Second-generation RV vectors encoding Cre and Flp retrogradely infect projection neurons, activate reporter expression and cause no apparent morphological abnormalities even up to a year after injection. **a**,**b**, Cortical neurons retrogradely labeled by second-generation RV vectors encoding either (**a**) Cre (7-d survival) or (**b**) Flp (14-d survival) recombinase injected into somatosensory thalamus of tdTomato reporter mice. **c**,**d**, Cortical neurons retrogradely labeled by second-generation RV vectors encoding Cre (**c**) or Flp recombinase (**d**) injected into the thalamus of reporter mice 1 year before perfusion. **e**,**f**, High-magnification images of dendrites and other fine processes of cortical neurons from the same sections imaged for **c** and **d**, showing apparently normal morphology with a complete absence of decomposition, blebbing or other abnormalities. These results indicate (i) that second-generation RV vectors are capable of expressing recombinases at levels sufficient to activate downstream transgene expression in readily available reporter mice; (ii) that second-generation RV vectors are capable of efficient retrograde infection of projection neurons; (iii) that the new vectors can be used to express different recombinases, allowing a variety of potential intersectional applications; and (iv) that the new vectors do not appear to cause cytotoxicity even on time scales comparable to the lifetime of the animal. Experiments in this figure were performed in 2 or 3 animals per condition, with similar results in all cases per condition. Scale bar in **a**–**d**, 250 µm; scale bars in **e**,**f**, 5 µm.

would nevertheless be sufficient to achieve site-specific recombination in genomic reporter alleles in reporter mouse lines.

We show that these new ('second-generation' or 'ΔGL') viral vectors can be used to express both Cre and Flp recombinases at levels sufficient to effect reporter gene expression in widely available reporter mice and in wild-type animals when used in combination with Cre-dependent adeno-associated viral (AAV) vectors, that the new vectors retain the first generation's characteristic ability to retrogradely infect projection neurons, and that targeted neurons appear morphologically normal up to a year postinjection. Using whole-cell recording in slices containing retrogradely targeted basolateral amygdala neurons, we show that transduced neurons exhibit normal membrane properties at 2 months postinjection. We use longitudinal two-photon structural and functional imaging in vivo in mouse primary visual cortex to show that targeted neurons exhibit no signs of toxicity and that responses to visual stimuli remain stable for at least 4 months, the longest time point in our dataset. Finally, we find that the new RV vector class has broader tropism for corticocortical projections than two other viral vector species commonly used for retrogradely targeting projection neurons.

This new class of vectors is immediately useful as a means of retrogradely targeting projection neurons to express Cre or other recombinases with no apparent toxic effects, allowing systematic selection of different classes of neurons for nonperturbative long-term anatomical or physiological study. This work also lays the foundation for the construction of a future second-generation monosynaptic tracing system that will leave transsynaptically transduced neurons alive and healthy indefinitely.

RESULTS

Testing in cell culture. We began by testing our hypothesis that *L* deletion would reduce vector expression to trace levels. Because genes in the rabies viral genome are expressed at levels that decrease with their positional order in the genome[23,26,28], we made and tested two variants of ΔGL rabies virus encoding enhanced green fluorescent protein (EGFP)[29]. In the first, RVΔGL-1EGFP, the *EGFP* gene was inserted in the highest-expressing locus, at the beginning of the genome before the remaining viral genes (note that the numbers in the vector names refer to the position of the transgene with respect to those of the other genes in the viral genome). In the second, RVΔGL-4EGFP, the *EGFP* gene was inserted in the lowest-expressing locus, at the end of the viral genome. Histograms of EGFP fluorescence in HEK 293T cells show that, whereas first-generation vectors encoding EGFP cause very bright fluorescence in infected cells (Fig. 1d; cf. uninfected negative control in Fig. 1c), second-generation vectors encoding EGFP (Fig. 1e,f) caused cells to express so little EGFP as to be nearly indistinguishable from uninfected controls, although anti-GFP immunostaining (Fig. 1c–e) confirmed that EGFP was indeed present at low levels. This was true whether the EGFP gene was inserted in the highest-expressing (Fig. 1e) or lowest-expressing (Fig. 1f) locus in the vector genome, indicating that *L* deletion indeed reduced gene expression to levels far below those of first-generation vectors, confirming our expectations.

However, these results raised the possibility that *L* deletion could reduce transgene expression so much that it would render the new vectors useless for neurobiological applications. Our next step was therefore to test whether second-generation RV vectors encoding a recombinase, as opposed to a fluorophore, are capable of expression at levels sufficient to activate reporter gene expression when used in the presence of a suitable recombinase-dependent reporter construct. We constructed two ΔGL vectors encoding Cre recombinase[30], the first (RVΔGL-1Cre) with the *Cre* gene inserted into the highest-expressing locus and the second (RVΔGL-4Cre) with it inserted into the lowest-expressing locus. We tested the viruses on a reporter cell line that expresses EGFP following Cre recombination, and the results were encouraging. Whereas uninfected control cells were not fluorescent (Fig. 1g), cells infected with either of the ΔGL vectors fluoresced brightly (Fig. 1h,i), indicating successful recombination of the reporter cells' EGFP expression cassette by viral expression of Cre. Because even RVΔGL-4Cre, the virus with the *Cre* gene in the lowest-expressing locus, was able to recombine the reporter cassettes, we used this version for the subsequent in vivo assays and refer to it simply as 'RVΔGL-Cre' below.

Anatomical testing in vivo. For our tests of the new class of vectors in vivo, we had three primary questions. (i) Are ΔGL vectors encoding recombinases capable of causing reporter expression in brains? (ii) Are the new vectors retrogradely infectious like the first-generation ones, so that projection neurons can be selectively targeted? (iii) Do the new vectors leave infected neurons alive and apparently healthy, and if so for how long?

Our in vivo experiments gave positive results on all three counts. To test the versatility of the new ΔGL vector class, we constructed two versions: the Cre-encoding vector RVΔGL-Cre, described above, and RVΔGL-Flpo, encoding Flp recombinase[31,32]. We injected these vectors into the somatosensory thalamus in mice of two reporter strains expressing the red fluorophore tdTomato[33] after reporter cassette recombination by the corresponding recombinase (see Methods). Note that all vectors described in this paper are

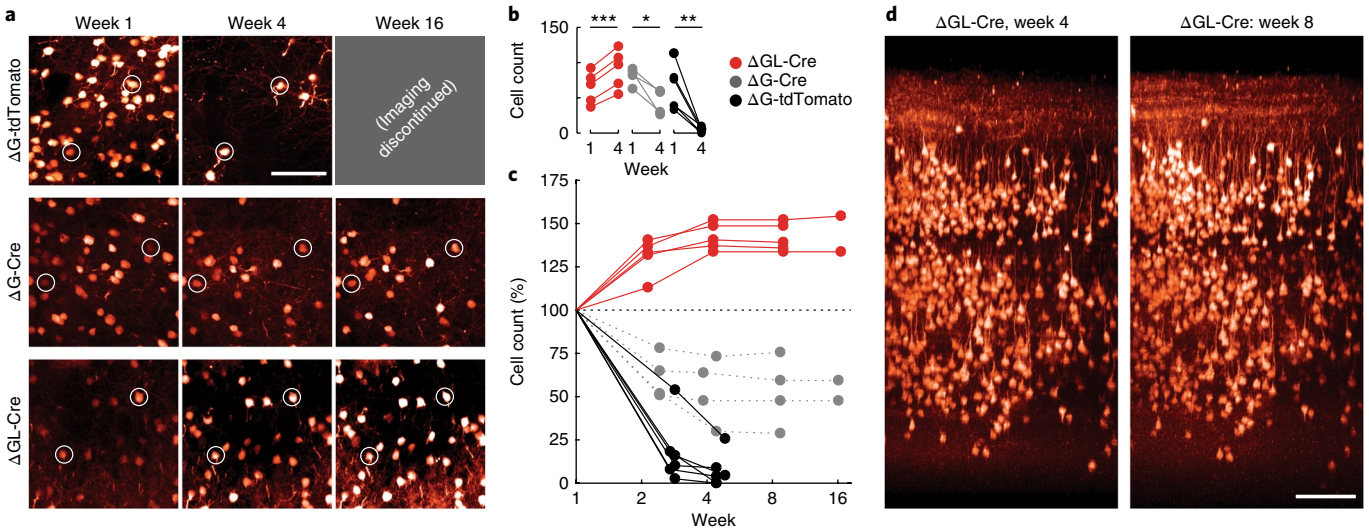

Fig. 3 | Longitudinal two-photon structural imaging shows that cortical neurons transduced with second-generation RV vectors remain alive and structurally normal for at least 4 months. a, Example two-photon FOVs transduced with first-generation RV encoding tdTomato (top row), first-generation RV encoding Cre in a tdTomato reporter mouse (middle row) and second-generation RV encoding Cre in a tdTomato reporter mouse (bottom row), at 1 week (left), 4 weeks (middle) and 16 weeks (right) after injection. Images within each column are of the same FOV imaged at the different time points. Two cells surviving across all time points for each animal are circled as fiducial markers. As seen in the top row, a first-generation RV encoding tdTomato kills almost all infected cells within 4 weeks of infection, in agreement with earlier work with similar vectors. Imaging was therefore not continued past 4 weeks for these mice. As seen in the middle row, a first-generation RV encoding Cre (as opposed to a fluorophore) kills only about half of infected neurons over the first few weeks. As seen in the bottom row, none of the neurons visibly labeled by the second-generation RV disappear over time. **b**, Population data for all structural FOVs in the study, comparing absolute cell counts between weeks 1 and 4. There is a significant increase in labeled ΔGL-Cre neurons (red; 5 FOVs; two-sided paired $t_4 = 11.3$, $^{***}P = 3.5 \times 10^{-4}$) and significant die-off in both ΔG-Cre (gray; 4 FOVs; paired $t_3 = 4.47$, $^{*}P = 0.021$) and ΔG-tdTomato conditions (black; 6 FOVs; paired $t_5 = 4.73$, $^{**}P = 5.2 \times 10^{-3}$). **c**, Percentage of visible labeled cells over time, relative to the number visible at 1 week postinjection, for each of the three viruses; connected sets of dots represent counts obtained from the same FOV within the same brain at the different time points. Cells labeled by first-generation RV encoding tdTomato (black) have almost entirely disappeared by 4 weeks postinjection. Cells labeled by first-generation RV encoding Cre (gray) have in many cases disappeared by 4 weeks, but approximately half remain and survive even to 8 weeks. Cells labeled by second-generation RV encoding Cre (red) do not die at any point: the numbers of visibly labeled cells increase up to 4 weeks postinfection (presumably as previously subthreshold tdTomato levels accumulate to the level of detectability) and then remain constant for as long as imaging is continued and presumably for the lifetime of the animal. **d**, Example renderings of the same volume of cortex labeled by second-generation RV encoding Cre at two different imaging time points, 4 weeks and 8 weeks. Every neuron visible at 4 weeks is still present at 8 weeks. This was consistent across the five ΔGL-Cre cases. Scale bars, 100 μm.

coated with the native rabies virus envelope protein, which confers on first-generation rabies viral vectors the ability to retrogradely infect large numbers of neurons that project to the injection site[1].

The result of these thalamic injections was bright fluorescence in hundreds of corticothalamic neurons in layer 6 of overlying somatosensory cortex for both RVΔGL-Cre (Fig. 2a,c,e) and RVΔGL-Flpo (Fig. 2b,d,f). Even with short survival times (Fig. 2a,b), abundant cortical neurons were labeled. This indicated two notable facts: first, that RVΔGL-Cre and RVΔGL-Flpo are quite capable of activating reporter gene expression in common reporter mice and, second, that second-generation RV vectors efficiently and retrogradely infect projection neurons, as do their first-generation counterparts[1]. Also, the fact that the efficacy of ΔGL vectors is not restricted to use with a single recombinase indicates that they will likely be useful for a variety of intersectional and simultaneous targeting approaches[34,35].

We also investigated whether the second-generation rabies viral vectors are compatible with recombinase-dependent AAV vectors, so that their use would not be restricted to applications in reporter mice. We found that this approach worked well in both mice and rats, as shown in Supplementary Figs. 1 and 2. This indicates that the vectors can be used in wild-type animals of multiple species for targeting expression of fluorophores and opsins to projection neurons selected on the basis of the locations of both their somata and axonal arborizations.

While these results demonstrate that the new second-generation rabies viral vectors retain the ability of first-generation ones to retrogradely infect projection neurons and that they are capable of causing recombinase-dependent expression of reporter genes, it remained to be seen to what degree *L* deletion achieved the main desired effect, namely, the elimination of the cytotoxicity that characterizes previous RV vectors. For a preliminary, qualitative answer to the question of preservation of the health of infected neurons, we simply conducted a series of thalamic injections of RVΔGL-Cre in Ai14 mice and RVΔGL-Flpo in Ai65F mice, killing them for analysis after increasing lengths of time. Even after leaving mice for an entire year after injection, brightly fluorescent cortical neurons were found in large numbers throughout layer 6 of somatosensory cortex (Fig. 2c,d). At higher magnification (Fig. 2e,f), dendritic spines and other fine processes were clearly intact and showed no blebbing or otherwise altered structures indicative of toxicity.

Longitudinal two-photon structural imaging. Although it appeared from these results that the second-generation rabies viral vectors do not kill neurons, there remained the possibility that only some of the labeled neurons survived over long periods, with others having died off. For a more rigorous examination, we conducted longitudinal two-photon imaging in vivo of labeled neurons in visual cortex to monitor individual neurons over the course

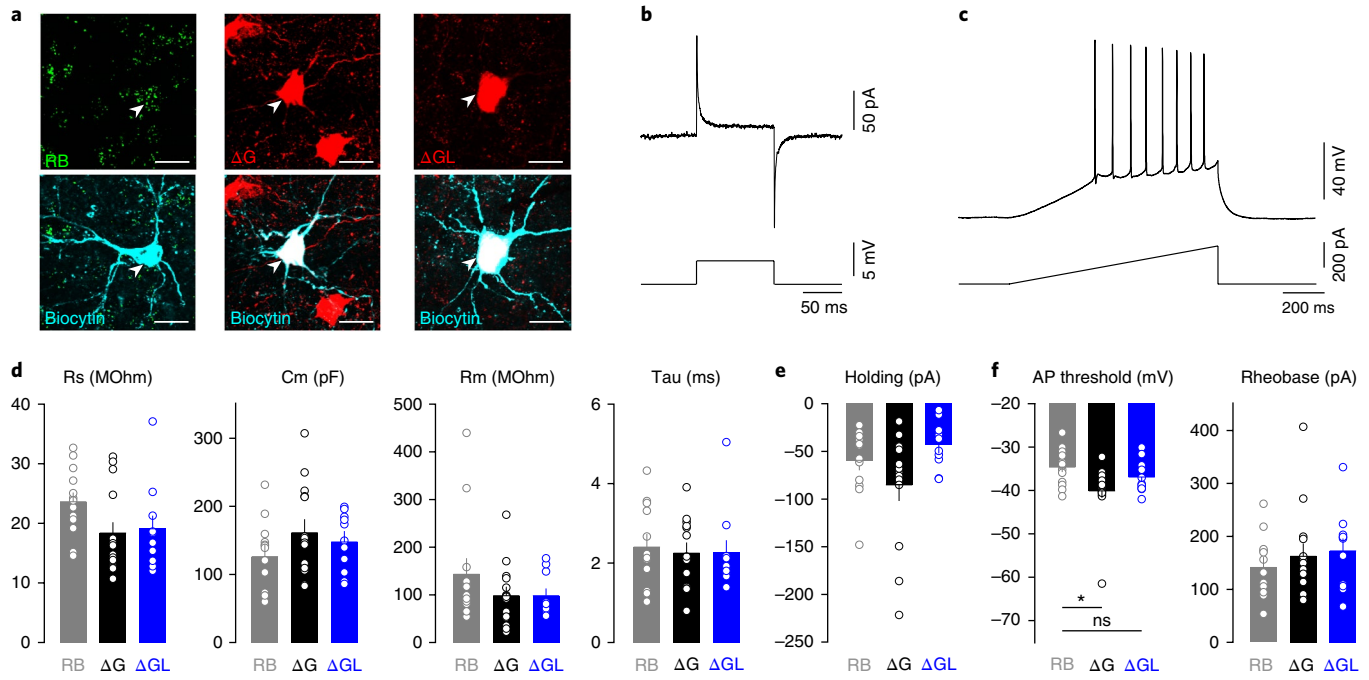

Fig. 4 | Membrane properties of neurons transduced with second-generation RV vectors remain normal for at least 8 weeks. a, Confocal images of basolateral amygdala neurons projecting to the nucleus accumbens and retrogradely labeled with either retrobeads (RB; left), first generation RV expressing Cre (ΔG; middle), or second-generation RV expressing Cre (ΔGL; right), imaged after targeted whole-cell patch-clamp electrophysiology. **b**,**c**, Representative traces of (**b**) a seal-test response in voltage-clamp and (**c**) a ramp test to induce action potential firing in current-clamp mode. **d**, The series resistance (Rs), capacitance (Cm), membrane resistance (Rm), and decay time constant (tau) were not different between the three experimental groups (one-way ANOVA; Rs: $F_{2,36}=2.51$, $P=0.096$; Cm: $F_{2,36}=1.35$, $P=0.27$; Rm: $F_{2,36}=1.38$, $P=0.26$; tau: $F_{2,36}=0.126$, $P=0.88$; $n=13$ RB, 15 ΔG and 11 ΔGL). **e**, Holding current at −70 mV was also not significantly different (one-way ANOVA; $F_{2,35}=3.14$, $P=0.056$; $n=13$ RB, 14 ΔG and 11 ΔGL). **f**, The action potential (AP) threshold was significantly more negative for the surviving cells transduced with the first-generation RV compared to cells containing RB, while cells transduced with the second-generation RV did not show a difference compared to RB-containing cells (one-way ANOVA; $F_{2,36}=4.29$, $^*P=0.021$, RB vs. ΔG: $P<0.05$, RB vs. ΔGL: $P>0.05$; $n=13$ RB, 15 ΔG and 11 ΔGL). The minimal current necessary to induce firing (rheobase) was not significantly different between the three groups (one-way ANOVA; $F_{2,36}=0.531$, $P=0.59$; $n=13$ RB, 15 ΔG and 11 ΔGL). All bar graphs display mean ± s.e.m. Experiments in this figure were performed in 6 animals each with similar results in all cases; n.s. indicates nonsignificance.

of months. This stringent test allowed us to see how many of the labeled neurons survived for long periods.

For these longitudinal imaging experiments, we compared the effects of the second-generation virus RVΔGL-Cre to those of two first-generation (ΔG) control viruses. The first control virus, RVΔG-tdTomato, contains the gene for tdTomato in its genome, while the second control virus, RVΔG-Cre, encodes Cre in its genome. We injected each virus into primary visual cortex of mice (Ai14-tdTomato reporter mice for the Cre-encoding viruses; wild-type C57BL/6J for RVΔG-tdTomato), then imaged the same fields of view (FOVs) with the same labeled neurons over multiple imaging sessions. This allowed us to track the fate of individual neurons for up to 4 months to obtain precise counts of the numbers of neurons that persisted as a function of time after infection (Fig. 3).

As expected, most neurons infected by the first-generation control vector RVΔG-tdTomato that were visible 1 week after injection were not seen after 4 weeks (Fig. 3a–c and Supplementary Video 1), consistent with previous reports of the rapid toxicity of first-generation RV vectors[1]. Imaging for the mice injected with this control virus was not continued after week 4 because there were very few neurons left to image, and most that remained showed dysmorphic processes and somata (Supplementary Fig. 3a–f).

We obtained more unexpected results with our other first-generation control virus, which encoded Cre instead of tdTomato. This virus killed a large fraction of infected neurons but by no means all of them (Fig. 3a–c and Supplementary Video 2). Approximately 50% of cells infected with RVΔG-Cre survived up to 4 months postinfection (Fig. 3b,c). This result, that simply encoding Cre instead of tdTomato made for a much less toxic first-generation rabies viral vector, is consistent with a previous report that some neurons infected with a replication-competent RV encoding Cre can survive infection, albeit with altered gene expression[36]. Nevertheless, even this less-toxic ΔG vector killed neurons over the first few weeks of imaging, and, as will be seen from the physiological results below (Figs. 4 and 5), we found signs that at least some of the surviving neurons had abnormal membrane and visual response properties.

In contrast to the complete or partial lethality of the first-generation control vectors, the second-generation vector RVΔGL-Cre did not kill neurons at all (Fig. 3a–c and Supplementary Video 3). The numbers of detected neurons actually increased over the first several imaging sessions and remained constant thereafter, presumably reflecting the gradual buildup of tdTomato fluorescence above detection threshold (note the relative dimness of the cells in the week 1 image compared to that in subsequent images). After the population of labeled cells stabilized, every cell in large imaged volumes (Fig. 3d and Supplementary Video 4) could be found at later time points, and we saw no cell death in any imaged FOV across the longitudinal study.

Ex vivo electrophysiology. While it was clear at this point that the second-generation vector was not killing neurons, it remained to be seen whether neurons transduced with the second-generation vector, and those remnant neurons that survived infection with its first-generation (RVΔG-Cre) counterpart, were physiologically

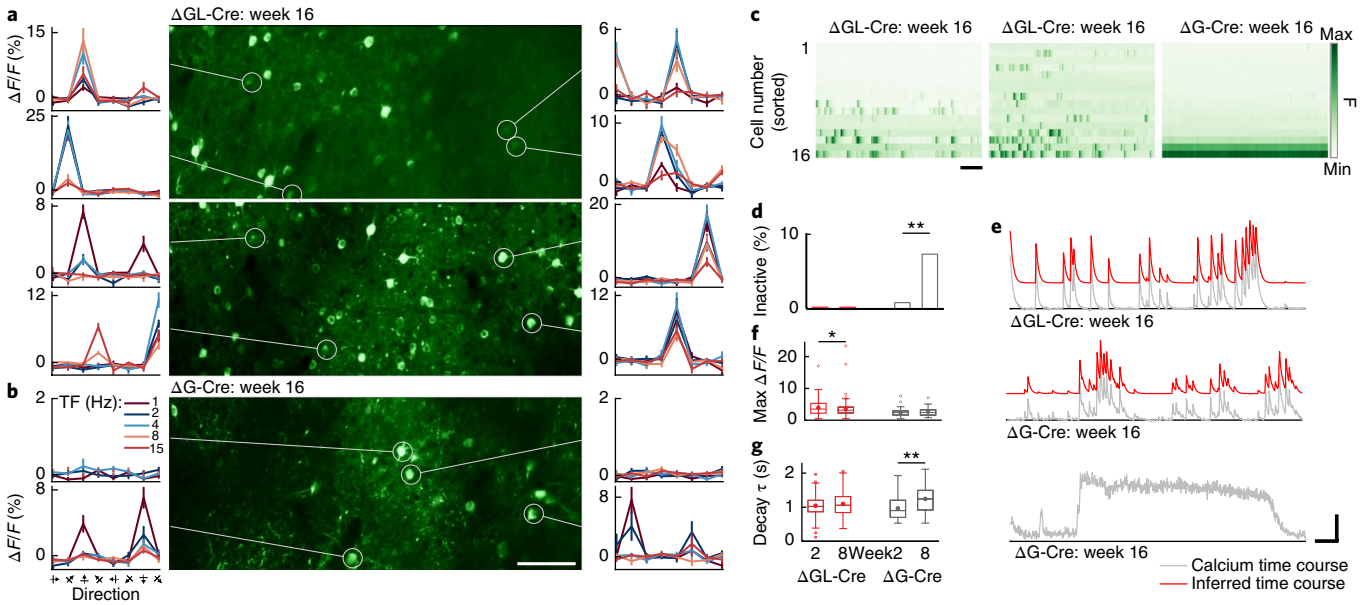

Fig. 5 | In vivo two-photon calcium imaging using GCaMP6f shows that cortical neurons transduced with second-generation rabies viral vectors retained stable visual response properties for at least 4 months. a, Calcium imaging from layer 2/3 of primary visual cortex (V1) in two Cre-dependent GCaMP6f reporter mice, 16 weeks after injection of second-generation virus RVΔGL-Cre. The FOVs (center) are maximum intensity projections of the imaging time series. The curves to the right and left of each FOV show example direction tuning curves of single cells (circled), obtained with drifting gratings presented at 8 directions of motion and 5 temporal frequencies (TF), repeated 15 times (mean $\Delta F/F \pm$ s.e.m.); color coding and axis labels on as in **b**; scale bar, 100 μm. Tuning curves were consistently responsive with clear direction preferences, as expected in V1. All cells bright enough to be segmented from the max projection showed at least spontaneous activity; bright-inactive cells were never seen in the RVΔGL-Cre cases. **b**, Calcium imaging from layer 2/3 of V1, 16 weeks after injection of first-generation virus RVΔG-Cre. While there are cells that show consistent direction preferences (lower curves) or spontaneous activity, there also appear bright cells with no activity of any kind (upper curves). **c**, Single-cell fluorescence time courses for the 16 cells with highest mean luminance in each FOV in **a** and **b** (normalized within FOV, sorted top to bottom from dimmest to brightest), showing the first 150 s of visual stimulation. Left and middle images (second generation, RVΔGL-Cre) show robust spontaneous and evoked activity. Right image (first generation, RVΔG-Cre) explicitly shows the pathology described in **b**, with the brightest cells being completely inactive, consistent with previous reports that cells with the highest baseline GCaMP fluorescence and filled-in appearance (no nuclear exclusion) often show altered or reduced activity[38,49]. Scale bar, 20 s. **d**, Proportions of bright-inactive cells across the RVΔGL-Cre (3 mice, 9 FOVs) and RVΔG-Cre (2 mice, 6 FOVs) populations, for weeks 2 and 8. Cells in the upper 50% of mean fluorescence for each FOV are shown, since poorly labeled GCaMP6f cells with no activity are often too dim to unambiguously segment, and the altered response properties associated with unhealthy RVΔG-Cre-labeled cells are observed in the brightest cells. None of the RVΔGL-Cre cells from week 2 (0 of 502 cells) or week 8 (0 of 717) were inactive, measured over the full 30 min of visual stimulation. Inactive cells were noticed as early as week 2 in the RVΔG-Cre condition (1 of 142, 0.7%) and increased significantly by week 8 (10 of 139, 7.2%; two-sample *z*-score proportion test, $z = 2.81$, $^{**}P = 5.2 \times 10^{-3}$). **e**, Example calcium time courses from week 16 (top left: RVΔGL-Cre; middle right and bottom left: RVΔG-Cre). Raw time courses (gray) of active cells can generally be approximated by an autoregressive (AR) process of order 1 (see Methods; inferred trace offset in red). The bottom RVΔG-Cre time course comes from an aberrant cell with a slow, sustained increase in brightness that is not well fit by the AR model and very sparse activity otherwise. This is distinct from the bright-inactive cells shown in **c** but may be part of the same progression toward inactivity or cell death. The two RVΔG-Cre examples come from the same FOV, within a hundred microns of each other, suggesting that the prolonged changes in fluorescence cannot be accounted for by *z*-motion artifacts. There were 13 such sustained-activity cells out of 46 (28.3%) segmented in the AR analysis of week-8 RVΔG-Cre cells. Vertical scale bar, Δ*F*/*F*, 3.0, 1.2, 0.3 for top, middle, and bottom traces, respectively. Horizontal scale bar, 20 s. **f**, Peak Δ*F*/*F* across the RVΔG-Cre and RVΔGL-Cre population, for weeks 2 and 8. The mean (± s.e.m.) of RVΔGL-Cre cells decreased significantly from week 2 (3.95 ± 0.17, $n = 191$) to week 8 (3.47 ± 0.14, $n = 247$; two-sided unpaired $t_{436} = 2.25$, $^{*}P = 0.025$) as baseline fluorescence gradually increased to final levels, but did not change significantly for the more rapidly expressing RVΔG-Cre cells between week 2 (2.46 ± 0.20, $n = 44$) and week 8 (2.71 ± 0.24, $n = 33$; $t_{75} = 0.81$, $P = 0.42$). **g**, Decay time constant (τ) of calcium transients across the RVΔG-Cre and RVΔGL-Cre population, for weeks 2 and 8. The mean τ of RVΔGL-Cre cells did not increase significantly from week 2 (1.07 ± 0.02 s, $n = 191$) to week 8 (1.12 ± 0.02 s, $n = 247$; two-sided unpaired $t_{436} = 1.72$, $P = 0.086$). For RVΔG-Cre cells, τ showed a pronounced increase from week 2 (0.99 ± 0.05 s, $n = 44$) to week 8 (1.27 ± 0.08 s, $n = 33$; $t_{75} = 3.31$, $^{**}P = 0.0014$). Sustained-activity cells were excluded from the analysis, so the large increase in τ in RVΔG-Cre cells likely underestimates the extent of changes in the RVΔG-Cre population. Data are represented as box plots showing mean (large points), median (horizontal line), 25th–75th percentile (boxes, interquartile range (IQR)), 1.5× IQR above or below 75th or 25th percentiles (whiskers), and outliers beyond this range (small points).

normal. We therefore injected first-generation (RVΔG-Cre) and second-generation (RVΔGL-Cre) vectors into the nucleus accumbens of Ai14 (tdTomato) reporter mice, along with fluorescent retrobeads in the contralateral nucleus accumbens of each mouse, then conducted whole-cell patch-clamp electrophysiology in slices from retrogradely labeled basolateral amygdala neurons at 8 weeks postinjection (Fig. 4). We found no significant difference in any measured membrane property between the neurons labeled with the second-generation vector versus the retrobead-labeled controls after 8 weeks of expression (Fig. 4d–f). In contrast, neurons that survived labeling with the first-generation vector had significantly more negative action potential thresholds than retrobead-labeled neurons (Fig. 4f). These data indicated that the second-generation vector RVΔGL-Cre did not produce detectable changes in the membrane properties of neurons, whereas the first-generation Cre-encoding control vector RVΔ

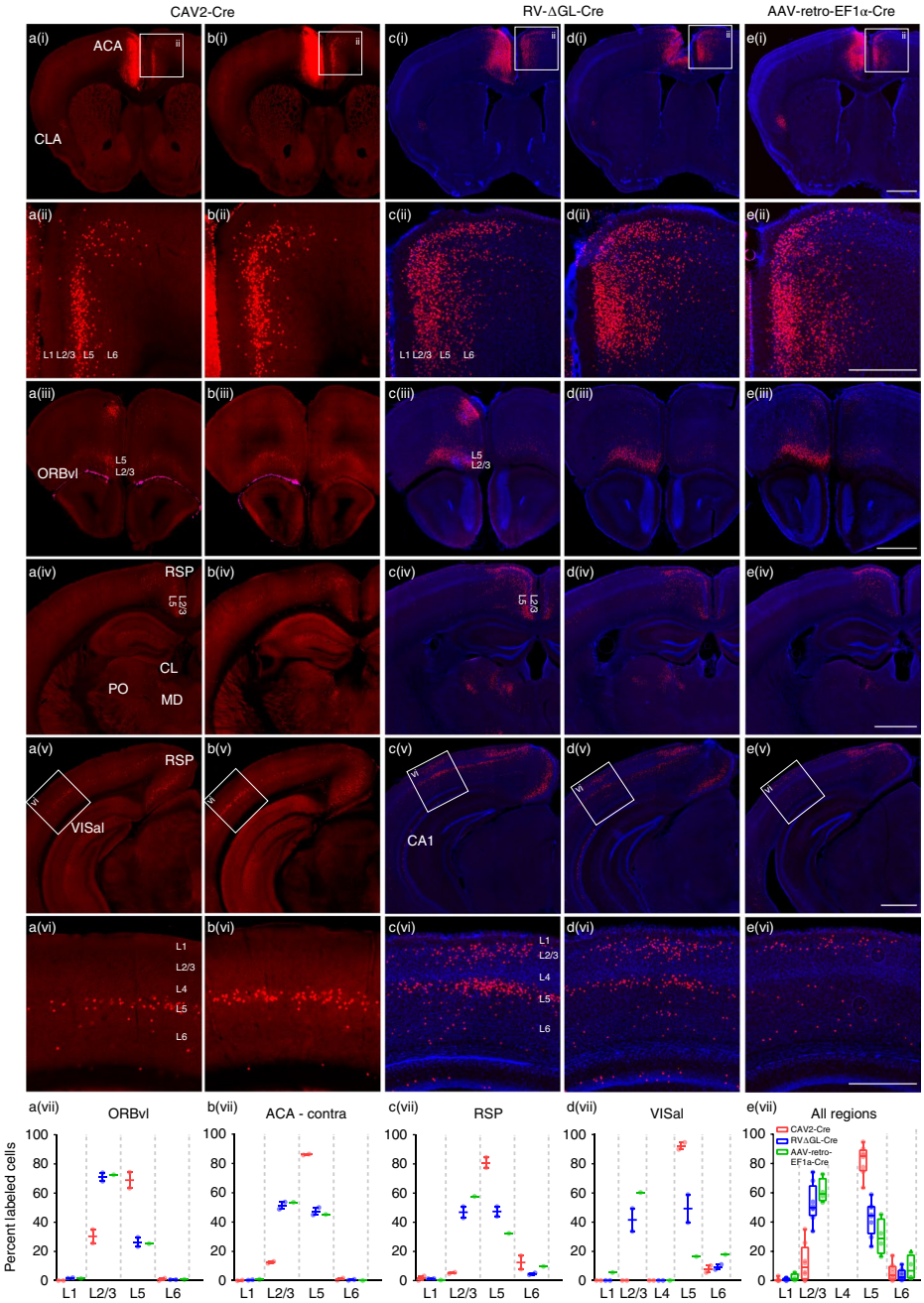

Fig. 6 | Second-generation RV vectors retrogradely infect more types of corticocortical cells than either CAV or rAAV2-retro vectors. a–e, CAV2-Cre (**a**,**b**), RVΔGL-Cre (**c**,**d**), or rAAV2-retro-EF1a-Cre (**e**) was injected into anterior cingulate area (ACA) of Ai75 mice, so that cells across the brain that provide input to ACA were labeled via Cre-induced nuclear tdTomato expression. The approximate center of the injection site for each experiment is shown in the top row (**i**, left side of images). Most brain regions containing retrogradely labeled cells from ACA were consistently identified across all three types of virus experiments, with at least one notable exception (CA1 contained labeled cells in RVΔGL-Cre, shown in **c**,**d**, row **v**). However, within the same areas, specifically in the cortex, we observed differences suggesting tropism or other biases in the specific types of neurons labeled. For example, labeled input cells in the contralateral ACA (boxes in row **i** indicate panels enlarged in row **ii**) were seen predominantly in layer 5 (L5) for CAV2-Cre (**a**,**b**, row **ii**), but were located more uniformly across layers with RVΔGL-Cre (**c**,**d**, row **ii**) and AAV-retro-EF1a-Cre (**e**, row **ii**). Similar differences between Cre^+ input cells across layers were observed in most cortical areas, including ventrolateral orbital cortex (ORBvl, row **iii**), retrosplenial cortex (RSP, rows **iv** and **v**), and anterolateral visual cortex (VISal, rows **v** and **vi**). Quantification of the number of labeled cells per layer indicated that, in all cases, CAV2-Cre labeling was biased toward L5 neurons, whereas RV-ΔGL-Cre resulted in input cells labeled across all layers providing long-range interareal inputs (L2/3, L5, L6; row **vii**). In contrast to RVΔGL-Cre and CAV2-Cre in VISal and RSP, AAV-retro-EF1a-Cre appeared to be biased toward L2/3, with only sparse labeling in L5 (**c**,**d**, row **vii**). Cre^+ input cells were also observed in subcortical structures, including several thalamic nuclei (for example, mediodorsal nucleus (MD), posterior complex (PO) and the central lateral nucleus (CL), seen in row **iv**, consistent with known connectivity of ACA. The more prominent labeling in RVΔGL-Cre and AAV-retro-EF1a-Cre cases in the thalamus (**c**–**e**, row **iv**) may be due to true differences in efficiency between viruses, or in the amount of viral uptake for each experiment; further experiments are necessary to explore this observation. Images in **a** and **b** were acquired by serial two-photon tomography. Images in **c**–**e** were acquired by epifluorescence microscopy and sections counterstained with DAPI (blue). Graphs in **a**–**d**, row **vii**, show the mean and full range of values (min to max, $n=2$ independent experiments for CAV2-Cre and RVΔGL-Cre; $n=1$ experiment for AAV-retro-EF1a-Cre). Boxplots in **e**, row **vii**, indicate the median and full range (min to max) in all four regions from **a**–**d**, row **vii** ($n=5$ independent experiments). Scale bars: rows **i** and **iii**–**v**, 1 mm; rows **ii** and **vi**, 500 µm.

G-Cre, even though it left some infected neurons alive, affected surviving cells' function.

Longitudinal two-photon functional imaging. To determine whether neurons transduced with the second-generation vector retained normal circuit response properties long-term, and to determine the degree to which those cells that survive transduction with the first-generation vector encoding Cre do as well, we conducted longitudinal in vivo two-photon calcium imaging of visual responses using GCaMP6f[37–39], again with repeated imaging of the same FOVs. We attempted to conduct long-term imaging of neurons infected with first-generation virus encoding GCaMP6f directly (RVΔG-4GCaMP6f) but found no responsive neurons beyond the 2-week time point when using this virus (see Supplementary Fig. 3g–i). We therefore injected either first-generation (RVΔG-Cre) or second-generation (RVΔGL-Cre) virus into the visual cortex of GCaMP6f reporter mice and imaged the visual response properties of transduced neurons to drifting gratings presented to the awake animal at time points up to four months.

At 16 weeks after injection, we found that neurons transduced with the second-generation vector had completely normal response properties. Those that responded to drifting gratings were well tuned to specific orientations (Fig. 5a), most showed spontaneous activity and there were no bright-but-inactive (bright–inactive) neurons in any FOV or time point (Fig. 5c–e and Supplementary Video 5). Tuning preferences of highly responsive individual neurons were stable over sessions spanning the entire 4 months of imaging (Supplementary Fig. 4). By contrast, neurons surviving infection with the first-generation vector RVΔG-Cre often had abnormal response properties. Many RVΔG-Cre-infected neurons displayed the bright–inactive phenotype (Fig. 5b–d) of very high fluorescence levels with no calcium transients or indication of spiking activity during visual stimulation. Some showed blebbing. Further (Fig. 5e), some cells showed occasional calcium transients followed by long, sustained increases in brightness that were distinct from the bright–inactive phenotype (see Supplementary Video 6 for examples of these pathologies). None of these aberrant physiological profiles were observed in any neurons labeled with the second-generation vector. As in the structural imaging experiments with tdTomato, neurons transduced with second-generation vector showed a gradual buildup of GCaMP6f, with the dimmer baseline fluorescence (F) reflected in higher signal amplitude $\Delta F/F$ at the earliest time points (Fig. 5f). Excluding cells with gross pathologies like bright–inactivity and sustained activity from the analysis, the population of neurons infected with the first-generation vector also showed a tendency toward more 'sluggish' calcium dynamics, with a large mean increase (29.1%) in the decay-time constant (τ) of calcium transients between the 2-week and 8-week imaging sessions (Fig. 5g). By contrast, neurons labeled with the second-generation vector showed stable time constants with no significant change in τ. All of these results indicate that the neurons labeled with the second-generation vector retained stable response properties at 8 and 16 weeks postinjection, whereas neurons infected with the first-generation vector, even when they survived for long durations, showed substantial changes and dysfunction over time.

Comparison to other vector species. As a final characterization, we conducted a direct comparison in vivo of the retrograde transduction ability of our second-generation rabies virus to two other viral species used for this application: canine adenovirus type 2 (CAV2)[40] and the newly developed rAAV2-retro[41]. We injected each of the three viruses in the anterior cingulate cortex of Ai75 reporter mice, in which nuclear-localized tdTomato is expressed following Cre recombination (Fig. 6). While all three viruses retrogradely labeled many cells in primary visual cortex, CAV2-Cre exhibited a pronounced preference for layer 5 cells, whereas rAAV2-retro labeled many cells in upper and lower layers but very few in layer 5. In contrast, RVΔGL-Cre labeled many cells in all cortical areas. Injections of the three vectors in other cortical areas showed similar results (Supplementary Fig. 5). These data are consistent with previous reports of both CAV2-Cre[42] and rAAV2-retro[41] having strong tropisms for particular cell types over others (in projections other than the ones examined here) and suggest that tropism may be less of an issue with second-generation RV than with these other two vector species.

DISCUSSION

Here we have introduced a class of RV vectors that do not cause any detectable structural or functional abnormalities in transduced neurons, in stark contrast to their first-generation counterparts. We have shown that these second-generation RV vectors encoding either Cre or Flp recombinase also are effective at causing reporter-gene expression both in cell culture and in vivo in readily available reporter mouse lines and in wild-type animals with reporter AAVs, that they retain first-generation vectors' ability to efficiently retrogradely transduce projection neurons far from the injection site, with wide tropism, and that these retrogradely transduced neurons appear morphologically and physiologically normal even at the longest time points examined. We expect that this new class of vectors will be a useful new tool for neuroscientists investigating neurons selected on the basis of their extrinsic projections.

Requirements for second-generation monosynaptic tracing. Given that these second-generation RV vectors do not structurally or functionally perturb neurons over any time scale examined and can be used to express recombinases in retrogradely infected projection neurons, an exciting potential application for this new class of vectors would be monosynaptic tracing. Monosynaptic tracing with first-generation RV vectors already allows neurons directly presynaptic to a targeted neuronal population or single neuron to be labeled for short-term anatomical identification[3,4,9,35,43], optogenetic manipulation[8,44] or activity imaging[7,10], but the toxicity of first-generation RV vectors confines these experiments to short-term experiments. A monosynaptic tracing system based on the second-generation RV vectors should allow labeled presynaptic networks to be imaged or optogenetically manipulated for months or even years. First-generation monosynaptic tracing requires coexpression of the single deleted gene (G), while a second-generation monosynaptic tracing system will also require expression of the deleted polymerase gene (L). In some contexts, this is theoretically very simple. Single-cell monosynaptic tracing, for example, currently entails introduction into single neurons, via a patch pipette, a mixture of plasmids encoding G, the receptor TVA (for allowing entry of the EnvA-enveloped RV into the targeted neuron) and a fluorophore to mark the targeted cell[4,5,7,10]. Second-generation RV would only require inclusion of a fourth plasmid, encoding L. While such direct transfection of single cells is the conceptually simplest implementation of monosynaptic tracing, the much more accessible and widely adopted approach is to label inputs to groups of neurons, using Cre or Flp mouse lines in combination with adeno-associated 'helper viruses' that express G, TVA and a fluorophore in the recombinase-expressing cells. This approach has allowed, for example, whole-brain mapping of inputs to dopaminergic neurons in the midbrain[6] and noradrenergic neurons in the locus coeruleus[45]. Adaptation of the helper virus approach to a second-generation version is, in principle, also straightforward. However, simply including an L-expressing AAV vector in the mix is problematic, because, at 6 kb in length, L exceeds the packaging capacity of AAV[46,47]. Alternative approaches currently being pursued include generating L-expressing mouse lines and splitting the polymerase into two complementary halves, each within the packaging capacity

of AAV. An aspect of RV biology that is likely to be very helpful to these efforts is the fact that the polymerase gene is expressed at very low levels by wild-type rabies virus, much lower than those of the other four viral genes, including G[26,48]. Achieving sufficient expression levels of L from the complementing systems—whether through direct transfection, genomic alleles or helper viruses—therefore appears unlikely to be a problem.

Methods

Methods, including statements of data availability and any associated accession codes and references, are available at https://doi.org/10.1038/s41593-018-0091-7.

Received: 9 July 2017; Accepted: 14 January 2018;
Published online: 5 March 2018

References

1. Wickersham, I. R., Finke, S., Conzelmann, K. K. & Callaway, E. M. *Nat. Methods* **4**, 47–49 (2007).
2. Wickersham, I. R. et al. *Neuron* **53**, 639–647 (2007).
3. Wall, N. R., Wickersham, I. R., Cetin, A., De La Parra, M. & Callaway, E. M. *Proc. Natl. Acad. Sci. USA* **107**, 21848–21853 (2010).
4. Marshel, J. H., Mori, T., Nielsen, K. J. & Callaway, E. M. *Neuron* **67**, 562–574 (2010).
5. Rancz, E. A. et al. *Nat. Neurosci.* **14**, 527–532 (2011).
6. Watabe-Uchida, M., Zhu, L., Ogawa, S. K., Vamanrao, A. & Uchida, N. *Neuron* **74**, 858–873 (2012).
7. Wertz, A. et al. *Science* **349**, 70–74 (2015).
8. Tian, J. et al. *Neuron* **91**, 1374–1389 (2016).
9. Wallace, M. L. et al. *Neuron* **94**, 138–152.e5 (2017).
10. Rompani, S. B. et al. *Neuron* **93**, 1519 (2017).
11. Liu, K. et al. *Nature* **548**, 582–587 (2017).
12. Chung, S. et al. *Nature* **545**, 477–481 (2017).
13. Dölen, G., Darvishzadeh, A., Huang, K. W. & Malenka, R. C. *Nature* **501**, 179–184 (2013).
14. Kiritani, T., Wickersham, I. R., Seung, H. S. & Shepherd, G. M. *J. Neurosci.* **32**, 4992–5001 (2012).
15. Kress, G. J. et al. *Nat. Neurosci.* **16**, 665–667 (2013).
16. Namburi, P. et al. *Nature* **520**, 675–678 (2015).
17. Rajasethupathy, P. et al. *Nature* **526**, 653–659 (2015).
18. Yamawaki, N., Suter, B. A., Wickersham, I. R. & Shepherd, G. M. *Cold Spring Harb. Protoc.* **2016**, t090084 (2016).
19. Shin Yim, Y. et al. *Nature* **549**, 482–487 (2017).
20. Osakada, F. et al. *Neuron* **71**, 617–631 (2011).
21. Gong, Y. et al. *Science* **350**, 1361–1366 (2015).
22. Roland, B. et al. *eLife* https://doi.org/10.7554/eLife.16335.001 (2016).
23. Wickersham, I. R., Sullivan, H. A. & Seung, H. S. *Nat. Commun.* **4**, 2332 (2013).
24. Reardon, T. R. et al. *Neuron* **89**, 711–724 (2016).
25. Ciabatti, E., González-Rueda, A., Mariotti, L., Morgese, F. & Tripodi, M. *Cell* **170**, 382–392.e14 (2017).
26. Albertini, A. A., Ruigrok, R. W. & Blondel, D. *Adv. Virus. Res.* **79**, 1–22 (2011).
27. Madore, H. P. & England, J. M. *J. Virol.* **22**, 102–112 (1977).
28. Schnell, M. J., McGettigan, J. P., Wirblich, C. & Papaneri, A. *Nat. Rev. Microbiol.* **8**, 51–61 (2010).
29. Cormack, B. P., Valdivia, R. H. & Falkow, S. *Gene* **173**, 33–38 (1996).
30. Sauer, B. & Henderson, N. *Proc. Natl. Acad. Sci. USA* **85**, 5166–5170 (1988).
31. Sadowski, P. D. *Prog. Nucleic Acid Res. Mol. Biol.* **51**, 53–91 (1995).
32. Raymond, C. S. & Soriano, P. *PLoS ONE* **2**, e162 (2007).
33. Shaner, N. C. et al. *Nat. Biotechnol.* **22**, 1567–1572 (2004).
34. Fenno, L. E. et al. *Nat. Methods* **11**, 763–772 (2014).
35. Schwarz, L. A. et al. *Nature* **524**, 88–92 (2015).
36. Gomme, E. A., Wirblich, C., Addya, S., Rall, G. F. & Schnell, M. J. *PLoS. Pathog.* **8**, e1002971 (2012).
37. Ohki, K., Chung, S., Ch'ng, Y. H., Kara, P. & Reid, R. C. *Nature* **433**, 597–603 (2005).
38. Chen, T. W. et al. *Nature* **499**, 295–300 (2013).
39. Ohki, K. & Reid, R. C. *Cold Spring Harb. Protoc.* **2014**, 402–416 (2014).
40. Soudais, C., Laplace-Builhe, C., Kissa, K. & Kremer, E. J. *FASEB J.* **15**, 2283–2285 (2001).
41. Tervo, D. G. et al. *Neuron* **92**, 372–382 (2016).
42. Senn, V. et al. *Neuron* **81**, 428–437 (2014).
43. Kohara, K. et al. *Nat. Neurosci.* **17**, 269–279 (2014).
44. Xu, C. et al. *Cell* **167**, 961–972.e16 (2016).
45. Schwarz, L. A. & Luo, L. *Curr. Biol.* **25**, R1051–R1056 (2015).
46. Wu, Z., Yang, H. & Colosi, P. *Mol. Ther.* **18**, 80–86 (2010).
47. Dong, B., Nakai, H. & Xiao, W. *Mol. Ther.* **18**, 87–92 (2010).
48. Finke, S., Cox, J. H. & Conzelmann, K. K. *J. Virol.* **74**, 7261–7269 (2000).
49. Tian, L. et al. *Nat. Methods* **6**, 875–881 (2009).

Acknowledgements

S.C. thanks D. Williams and S. de Vries for software, A. Cheng and N. Orlova for hardware construction, and R. D'Aleo and N. Ouellette for experimental assistance. J.A.H. thanks K.E. Hirokawa and P. Bohn for technical assistance. I.R.W. thanks W. Salmon for assistance with confocal imaging. The authors thank the founders of the Allen Institute for Brain Science, Paul G. Allen and Jody Allen, for their vision, encouragement and support. Research reported in this publication was supported primarily by the National Institute of Mental Health under award number U01MH106018 (BRAIN Initiative) to I.R.W. and in part by the National Institute on Aging under award number R01AG047589 to J.A.H. and the National Eye Institute under award numbers R01EY010115 and R01EY018742 to R.C.R. K.M.T. was supported in part by a New York Stem Cell Foundation Robertson Investigator award and McKnight Scholar Award, and G.G.C. was supported by a JFDP fellowship and a NARSAD Young Investigator Award. The content of this paper is solely the responsibility of the authors and does not necessarily represent the official views of the National Institutes of Health.

Author contributions

S.C. helped design experiments, performed two-photon imaging and quantified and analyzed the results, assisted by B.J.M. and overseen by R.C.R. H.A.S. produced all RV vectors, assisted by S.D. R.X. and Y.H. cloned all RV vectors. T.K.L. and N.E.L. injected RV vectors in vivo for anatomical experiments in reporter mice and, in combination with FLEX AAV in rats; they also processed the tissue for these experiments, assisted by J.E.M. T.K.L. also conducted confocal imaging. K.R.B. bred mice for the anatomical experiments and assisted with cloning viral vectors. G.A.M., A.B., and G.G.C. performed ex vivo physiological recordings, G.G. injected vectors and retrobeads for these ex vivo experiments, and K.M.T. oversaw and helped plan them. J.D.W. and J.A.H. conducted experiments (injections, histology, imaging and analysis) comparing RV with rAAV2-retro and CAV2-Cre and using RV in combination with FLEX AAV in mice; H.Z. oversaw these comparative and combinatorial experiments, and S.Y. and A.C. produced the AAV2-retro stocks. I.R.W. conceived and designed the study; I.R.W. and S.C. wrote the manuscript with input from other authors.

Competing interests

The authors declare no competing interests.

Additional information

Supplementary information is available for this paper at https://doi.org/10.1038/s41593-018-0091-7.

Reprints and permissions information is available at www.nature.com/reprints.

Correspondence and requests for materials should be addressed to I.R.W.

Publisher's note: Springer Nature remains neutral with regard to jurisdictional claims in published maps and institutional affiliations.

Methods

Animals. All experimental procedures related to the use of mice were conducted according to NIH guidelines. Experiments performed at the Allen Institute were approved by the Institutional Animal Care and Use Committee (IACUC) of the Allen Institute for Brain Science. Experiments performed at MIT were approved by the MIT Committee for Animal Care (CAC). Animals were housed singly postinjection, and were kept on a normal light/dark cycle for all experiments except awake two-photon imaging.

Cloning. Expression vectors for rabies viral genes and the T7 polymerase were made by cloning the *N*, *P*, *G* and *L* genes from pTIT-N, pTIT-P, pTIT-L[50], pTIT-G[51], and pCAGGS-T7[52] into pCAG-GFP[53] (Addgene #11150) to make pCAG-B19N (Addgene #59924), pCAG-B19P (Addgene #59925), pCAG-B19G (Addgene #59921), pCAG-B19L (Addgene #59922) and pCAG-T7pol (Addgene #59926).

The Flp reporter construct pLV-CAG-F14F15S-Switch was made by cloning into pCSC-SP-PW-GFP[54] (Addgene #12337) the CAG promoter[55] and a Flp-dependent 'FLEX'[56] construct consisting of pairs of compatible FRT sites flanking a back-to-back fusion of the reverse-complemented gene for TagRFP-T[57] immediately followed by the forward gene for EGFP.

First-generation vector genome plasmids were made by insertion of the *tdTomato*[53] or mammalian codon-optimized *Cre*[58] gene in place of the *EGFP* gene in pRVΔG-4GFP (a.k.a. cSPBN-4GFP (Addgene #52487) to make pRVΔG-4tdTomato (Addgene #52500), pRVΔG-4Cre (Addgene #98034) and pRVΔG-4GCaMP6f (Addgene #98035; the '4' in the plasmid/virus names refers to the position of the transgene in the viral genome, following the convention introduced by Wickersham et al.[59]).

Second-generation vector genome plasmids were made by complete deletion of the polymerase gene as well as the *G–L* intergenic sequence from cSPBN-4GFP and pRVΔG-1EGFP[23], with and without replacement of the *EGFP* gene with the *Cre* or *Flpo* genes, by seamless cloning (In-Fusion, Takara), resulting in pRVΔGL-4EGFP (Addgene #98036), pRVΔGL-1EGFP (Addgene #98037), pRVΔGL-1Cre (Addgene #98038), pRVΔGL-4Cre (Addgene #98039) and pRVΔGL-4Flpo (Addgene #98040).

Rabies viral vector production and titration. First-generation rabies viral vectors (RVΔG-EGFP, RVΔG-tdTomato and RVΔG-Cre) were made as described[60]. Briefly, HEK 293T cells (ATCC CRL-11268) were transfected with expression vectors for the ribozyme-flanked viral genome (pRVΔG-4EGFP, pRVΔG-4tdTomato or pRVΔG-4Cre), rabies viral genes (pCAG-B19N, pCAG-B19P, pCAG-B19G and pCAG-B19L) and the T7 polymerase (pCAG-T7Pol). Supernatants were collected 4–7 d after transfection, filtered and pooled, then passaged 3–4 times on BHK-B19G2 cells[59] at a multiplicity of infection of 2–5. Purification, concentration and titration were done as described[59], with the Cre reporter cell line 293T-Switch2[61] used for titrating RVΔG-Cre.

Production of second-generation rabies viral vectors (RVΔGL-EGFP, RVΔGL-Cre and RVΔGL-Flpo) proceeded similarly but with the supernatants from the transfection plates passaged not on BHK-B19G cells but on HEK 293T cells transfected with pCAG-B19G and pCAG-B19L. Purification, concentration and titration were as described[59], with RVΔGL-Cre titered on 293T-Switch2 cells and RVΔGL-FlpO titered on HEK 293T cells transfected with the Flp reporter construct pLV-CAG-F14F15S-Switch.

Immunostaining, imaging and flow cytometric analysis of HEK 293T cells. HEK 293T cells infected with serial dilutions of RVΔG-EGFP and RVΔGL-EGFP, as described[59], were fixed with 4% paraformaldehyde, permeabilized with 0.05% Triton-X (Sigma) in 5% normal donkey serum (Jackson Immuno, #017-000-121), then incubated with 1:1,000 chicken anti-GFP polyclonal primary antibody (Aves Labs, GFP-1020) for 1 h followed by washing and incubation with 1:500 Alexa Fluor-594-conjugated donkey anti-chicken secondary antibody (Jackson Immuno, #703-585-155). Images were collected on a Zeiss 710 confocal microscope, and flow cytometric analysis was conducted as described[59].

Mouse thalamic injections, histology, & confocal imaging. Mouse lines used for thalamic injections were the Cre-dependent tdTomato reporter line Ai14[62] (Jackson Laboratory #007908) and the Flp-dependent tdTomato reporter line Ai65F, produced by crossing the Cre- and Flp-dependent tdTomato double-reporter line Ai65D[63] (Jackson Laboratory 021875) to the Cre deleter line Meox2-Cre[64] (Jackson Laboratory 003755), so that only Flp is required for expression of tdTomato.

We injected 50–100 nL of viral vector solution into ventral posteromedial nucleus (−1.90 mm AP, 1.57 mm LM, 3.66 mm DV; all stereotaxic coordinates are with respect to bregma) of anesthetized adult mice (Ai14 for RVΔGL-Cre or Ai65F for RVΔGL-Flpo) using a stereotaxic instrument (Stoelting Co.) and custom injection apparatus consisting of a hydraulic manipulator (MO-10, Narishige) with headstage coupled via custom adaptors to a wire plunger advanced through pulled-glass capillaries (Wiretrol II, Drummond) backfilled with mineral oil and frontloaded with viral vector solution.

Seven to 398 d following virus injection, mice were perfused transcardially with 4% paraformaldehyde in phosphate-buffered saline. Brains were postfixed in 4% paraformaldehyde overnight at 4 °C and cut into 50-µm sections on a vibrating microtome (VT-1000S, Leica). Mounted sections were imaged on a LSM 710 confocal microscope (Zeiss).

Rat intersectional injections, histology and confocal imaging. Adult Long-Evans rats (269–299 g) were injected with both RVΔGL-Cre and a FLEX AAV using the custom injection apparatus described above. For labeling thalamocortical neurons, 100 nL of RVΔGL-Cre were injected into barrel cortex (−1.44 mm AP, +5.40 mm LM, −3.00 mm DV) and 300 nL of AAV8-hSyn-DIO-mCherry (Addgene #50459) or AAV5-Syn-FLEX-rc[ChrimsonR-tdTomato] (Addgene #62723) were injected into ventral posteromedial nucleus (−3.50 mm AP, +3.00 mm LM, −6.00 mm DV) in the same surgery. For labeling corticothalamic neurons, 100 nL of RVΔGL-Cre were injected into ventral posteromedial nucleus, and 300 nL of AAV8-hSyn-DIO-mCherry (Addgene #50459) or AAV5-Syn-FLEX-rc[ChrimsonR-tdTomato] (Addgene #62723) were injected into barrel cortex in the same surgery. Twenty-one days following injection, rats were perfused, and their brains were sectioned and imaged on a confocal microscope as described above.

Surgical preparation and virus injections for two-photon imaging. Mouse lines used for in vivo two-photon imaging were the Cre-dependent tdTomato reporter line Ai14 for RVΔG-Cre and RVΔGL-Cre structural imaging studies; the Cre-/tTA-dependent GCaMP6f[58] reporter line Ai93[63] (Jackson Laboratory #024103) crossed with the tTA driver line Camk2a-tTA[65] (Jackson Laboratory #007004) for RVΔG-Cre and RVΔGL-Cre functional imaging studies; and C57BL/6 mice (Jackson Laboratory #000664) for all RVΔG-tdTomato and RVΔG-GCaMP6f experiments.

Adult mice (>P45; male and female) were anesthetized under isoflurane (3% induction, 1.25% maintenance, 100% O_2) and ketamine/xylazine (70 mg/kg, i.p.). An incision was made in the scalp and a headplate was implanted with Metabond (Parkell) using aseptic technique. A craniotomy (5-mm diameter) and durotomy were performed over left hemisphere V1 and higher visual areas (ML 3.1 mm, AP 1.3 mm from lambda), and a glass window was cemented over exposed cortex.

After allowing the mice a minimum of 7 d to recover from surgery, we mapped visual area boundaries with widefield intrinsic signal imaging of autofluorescence under 470-nm excitation[66,67]. The emitted fluorescence was collected by a 4× objective (Olympus, NA 0.28), long-pass filtered (500-nm cutoff) and recorded on a PCO.edge CMOS camera (60-Hz frame rate; 2,160×1,920 pixels). The awake, head-fixed animal was shown 7 retinotopic mapping conditions on an LCD screen (60-Hz refresh rate) positioned 25 cm from the contralateral eye. Each condition consisted of a circular patch (30° diameter) of square-wave drifting grating on a black background (100% grating contrast, 8 directions shown in quick succession, 0.05 cycles/degree, drifting at 4 Hz) for 5 s, followed by 15 s of black background. The conditions varied only in screen position (two rows of three evenly spaced patches each, spanning the screen, followed by a seventh patch in the center). The stimulus set was repeated 5 times. After downsampling the imaging data to 2 Hz, $\Delta F/F$ for each condition was calculated as the difference between fluorescence during the stimulation period (taken as the average signal of the first 4 s) and the blank period (9–20 s), divided by fluorescence during the blank, averaged over all repeats. This procedure clearly delineated the boundaries of visual areas V1, LM, PM and AL.

Using these intrinsic signal images, we targeted all injections to the part of V1 mapped to the center of the LCD screen. The animal was anesthetized under 1.25% isoflurane in 100% O_2 and the glass window removed. A replacement window with a predrilled 500- to 750-µm hole was secured over exposed cortex with silicone elastomer (Kwik-Cast, WPI). Virus solutions were titer-matched by diluting with HBSS (diluted titer for all viruses was approximately 5×10^9 infectious units/mL), and Alexa Fluor-594 hydrazide (30-µM final concentration; Thermo Fisher) was added as a contrast agent. Injections were done under two-photon visual guidance using glass micropipettes broken to a tip size of 7.5 µm. After advancing the micropipette through the hole in the window and down to >300 µm depth in cortex, we waited 5 min, then injected for 2.5–3 min at 80- to 100-mbar pressure, visually monitoring the spread of Alexa Fluor during the entire injection. After waiting an additional 5 min, we repeated the injection procedure. The temporary window was removed and a standard window was cemented over cortex before recovering the animal.

Structural two-photon imaging and data analysis. Imaging was done with the animal anesthetized under 1.25% isoflurane in 100% O_2. Eyes were protected with Puralube ointment and body temperature maintained at 37 °C. A week after virus injection, fields of view (FOVs) were chosen some distance away from the area of brightest tdTomato labeling, since relative sparseness was useful for counting cells. Two well-separated areas were chosen in each mouse, one near the edge of V1, the other either on the opposite edge of V1 or in a higher visual area (LM or PM; except in one mouse with a single V1 FOV). No systematic differences were observed in cell survival rates between V1 and higher visual areas, so all FOVs were treated as equal in the analyses.

Two-photon structural imaging was performed on a custom-built microscope with nonresonant galvanometric scanning mirrors (512×512 pixels, 1-Hz frame rate) coupled to a mode-locked Ti:sapphire laser (Chameleon Ultra II) emitting at 1,020 nm. Image acquisition was controlled with a modified version of ScanImage[68]. Laser power exiting the 16× water-immersion objective (Nikon, NA 0.8) varied between 30 and 70 mW, depending on depth. Two volumes were

imaged in each area at each time point: one at low magnification (600 × 600 µm per frame, from pial surface down to 300–600 µm, 1-µm spacing between frames), used to record labeling efficiency, for alignment checks and for the volume renders (for example, Fig. 2c); and a second, smaller volume (100–200 µm in z) taken at higher magnification (300 × 300 µm per frame, 1-µm spacing). The latter was used for cell counts. The main criterion for deciding how many frames to include in the high-magnification stacks was reducing somatic overlap when a maximum-intensity z-projection was taken of the stack, so that individual cells could be unambiguously identified in the projection. The max projections for different time points of an individual imaged area were aligned using TurboReg[69] in ImageJ. An affine transformation was generally appropriate, since slight cortical deformations did occur over 16 weeks. Each alignment was checked, with attention paid to dendritic processes and other unique identifiers. After alignment across time points, cell bodies were manually counted in Vaa3D[70]. Vaa3D was also used for full-volume renders of the low-magnification stacks. Images were pseudocolored for presentation in ImageJ.

Fifteen cell-counting FOVs from eight animals were followed over time: five RVΔGL-Cre FOVs from three animals; four RVΔG-Cre FOVs from two animals; and six RVΔG-tdTomato FOVs from three animals, giving us a total starting population of 1,025 cells. All FOVs and time points are shown in Fig. 3c. No injected animals that survived beyond 4 weeks were excluded, so statistical analyses of cell counts (paired t tests; Fig. 3b) were performed for all FOVs at weeks 1 and 4. Imaging was only terminated before 16 weeks in case of animal health reasons or death, or in the case of RVΔG-tdTomato because very few cells remained.

Functional two-photon imaging and data analysis. A week after virus injection, the center of the brightest GCaMP6 label in left-hemisphere V1 (assessed under conventional epifluorescence) was chosen as the imaging area. Two-photon functional imaging was performed using a custom-built, resonant-scanning microscope (30-Hz frame rate, 512 lines per frame) with the same objective and laser (at 940 nm) as in the structural imaging experiments. Laser power at the objective ranged from 50 to 150 mW. Calcium imaging data were acquired from three equally spaced planes in supragranular layers (100- to 200-µm deep). Surface vasculature provided coarse fiducial markers for finding the same FOVs in subsequent weeks. Radial vasculature and cell body images from averaged data taken in the first session provided a template for fine alignment. The animal was awake, head-fixed and free to run on a circular disk. No behavioral training or reward was given.

Visual stimuli were generated in python with custom software based on Psychopy[71] and shown on the same LCD screen as in the widefield mapping experiments. Each condition consisted of 2 s of a full-field sine-wave grating drifting in one direction, presented at 80% contrast with spatial frequency of 0.04 cycles/degree, followed by 1 s of uniform mean luminance (gray). All permutations of 8 directions (45° steps) and 5 temporal frequencies (1, 2, 4, 8 and 15 Hz) were shown, in randomized order. The complete set was repeated 15 times, for a total stimulation period of 30 min per FOV per session. Whole-frame registration based on cross-correlation was used to reduce motion artifacts, and data were downsampled to 4 Hz. Cells were then manually segmented, and single-cell fluorescence traces were extracted by averaging the fluorescence of all pixels masking the soma. The mean $\Delta F/F$ over the full 2 s of each stimulus condition was used to calculate orientation tuning curves, with background fluorescence (F) in $\Delta F/F$ taken as the value of the trace immediately preceding a condition, averaged over all conditions. The raw calcium traces from cells within individual FOVs (not across FOVs, given different imaging conditions across animals and time points) were sorted by mean fluorescence, and the quantification of bright–inactive cells was performed only on cells in the upper half of sorted brightness for each FOV, to distinguish abnormal, filled-in cells from cells that may have been healthy but quiescent.

To estimate time constants, the functional data were reprocessed using a constrained non-negative matrix factorization (CNMF) algorithm[72] with Python code provided by the authors. In the CNMF framework, the matrix encoding the complete spatiotemporal activity of a calcium imaging session is expressed as the product of a spatial matrix encoding the location of each neuron in the FOV and a temporal matrix encoding the time-varying fluorescence signal of each neuron. Notably, the framework imposes a model of calcium indicator dynamics that can be approximated as an autoregressive process of order p(AR(p)). Since GCaMP6f has a small rise time constant[38] relative to the length of our imaging time bin Δt, a first-order model AR(1) was appropriate for this dataset[72], in which the calcium impulse response following a spike is modeled by an instantaneous rise followed by a slowly decaying exponential function with a single decay time constant τ. The discrete AR(1) model of the calcium concentration dynamics $c(t)$ at time-steps $t = 1,\ldots T$, can be written as

$$c(t) = \gamma \times c(t-1) + s(t)$$

where $s(t)$ is the number of spikes estimated at time-step t and γ is an estimate of the discrete time constant. The decay time constant τ can then be calculated from γ using the relation:

$$\tau = -\Delta t / \log(\gamma)$$

Decay time constants were estimated for cells segmented with the CNMF package using data from the first 4 min of each imaging session. Only cells that had a peak inferred $\Delta F/F > 0.25$ with no plateaus of elevated fluorescence (for example, bottom trace in Fig. 5e), with some activity (no bright–inactive cells), and that were clearly imaged at their cell bodies and not apical dendrites (which generally exhibited different time constants than somatic signals), were included in the population analysis.

Seven animals were used in these functional imaging experiments (21 total FOVs): three RVΔGL-Cre cases, each imaged out to 16 weeks postinjection; two RVΔG-Cre cases, each imaged out to at least 8 weeks postinjection (with one imaged at 16 weeks); and two RVΔG-GCaMP6f cases, imaged out to only 4 weeks because of very few surviving cells (see Supplementary Supplementary Fig. 3). Since week 2 had brighter GCaMP6f labeling than week 1 in the two Cre conditions, population analyses over time (Fig. 5d,f,g) were done between weeks 2 and 8. Imaging termination criteria were the same as in the structural imaging experiments.

Whole-cell patch-clamp recordings. For brain slice electrophysiology recordings, 6 adult male Ai14 transgenic mice (aged 8 or 14 weeks) were used. Retrobeads (Lumafluor Inc.) or the first- or second-generation rabies viral vector encoding Cre recombinase was injected into the nucleus accumbens (NAc) at the following stereotaxic coordinates from bregma: +1.30 mm AP, +0.80 mm ML and −4.70 mm DV.

After 8 weeks, mice were anesthetized with 90 mg/kg sodium pentobarbital and perfused transcardially with 20 mL of artificial cerebrospinal fluid (ACSF, at ~4 °C) containing (in mM): 75 sucrose, 87 NaCl, 2.5 KCl, 1.3 NaH_2PO_4, 7 $MgCl_2$, 0.5 $CaCl_2$, 25 $NaHCO_3$ and 5 ascorbic acid. The brain was extracted and glued (Roti coll 1; Carh Roth GmbH, Karlsruhe, Germany) to the platform of a semiautomatic vibrating blade microtome (VT1200; Leica, Buffalo Grove, IL), which was placed in a slicing chamber containing modified ACSF at 4 °C. Coronal sections of 300 µm containing the NAc and BLA were collected and placed in a holding chamber filled with ACSF saturated with 95% O_2 and 5% CO_2, containing (in mM): 126 NaCl, 2.5 KCl, 1.25 NaH_2PO_4, 1.0 $MgCl_2$, 2.4 $CaCl_2$, 26.0 $NaHCO_3$ and 10 glucose. Recordings commenced at least 1 h following slicing, and the temperature was maintained at approximately 31 °C both in the holding chamber and recording chamber. All NAc injection sites were verified and imaged with a camera (Hamatsu Photonics K.K., Japan) attached to a microscope (BX51; Olympus, Center Valley, PA).

Recordings were made from visually identified neurons expressing tdTomato or containing retrobeads. Voltage- and current-clamp recordings of BLA neurons projecting to the NAc were conducted using glass microelectrodes (4–7 MΩ) shaped with a horizontal puller (P-1000, Sutter, CA) and filled with a solution containing (in mM): 125 potassium gluconate, 20 HEPES, 10 NaCl, 3 MgATP, 8 biocytin and 2 Alexa Fluor-350 (pH 7.33; 287 mOsm). Recorded signals were amplified using a Multiclamp 700B amplifier (Molecular Devices, Sunnyvale, CA). Analog signals were digitized at 10 kHz using a Digidata 1440 and recorded using pClamp10 software (Molecular Devices, Sunnyvale, CA). Oxygenated ACSF was perfused onto the slice via a peristaltic pump (Minipuls3; Gilson, Middleton, WI) at ~3 mL/min. The membrane properties of each cell were evaluated in voltage-clamp and current-clamp modes. The access resistance (Rs), membrane capacitance (Cm), membrane resistance (Rm) and time constant (tau) were calculated from a membrane seal test conducted in voltage-clamp mode, in which 100-ms, 5-mV voltage steps were delivered at a frequency of 5 Hz. We also measured the holding current at a holding potential of −70 mV and calculated the current/voltage relationship in voltage-clamp using a series of 200-ms voltage steps, deviating from the −70 mV holding potential by −30, −25, −20, −15, −10, −5, 0, +5, 10, 15, 20, 25, 30, 35, and 40 mV. In order to evaluate the action potential threshold and rheobase, a 1-s, 300- to 750-pA current ramp was delivered in current-clamp mode. Finally, to evaluate the relationship between injected current and firing frequency, we delivered a series of 2-s current pulses in current-clamp, in which the first pulse was 50 pA above the holding current required to keep the cell at −70 mV and each subsequent pulse increased by 25 pA to a maximum of 525 pA. Any significant changes in Rs or holding current were interpreted as signs of poor cell health and recordings were terminated. Offline analysis was performed using Clampfit 10.6.1.1 (Molecular Devices, Sunnyvale, CA) or Matlab R2013b (seal test analysis). Statistical significance was assessed with GraphPad Prism 6 (GraphPad Software, Inc.) using a one-way analysis of variance (ANOVA), with Neuman–Keuls post hoc tests where appropriate.

Comparative viral vector injections, imaging and quantification. CAV2-Cre with a titer of 1.0×10^{12} genome copies/mL was obtained from the Viral Vector Production Unit at the Universitat Autonoma de Barcelona and was produced from a vector enabling expression of Cre under control of the CMV promoter[73]. rAAV2-retro-Cre was generated at the Allen Institute by cotransfecting HEK 293T cells with pAAV-EF1a-Cre-WPRE-hGHpolyA, pHelper and pAAV2-retro[41], followed by iodixanol gradient purification. The Cre coding sequence, with the Kozak consensus sequence of GCCGCCACC, was inserted into the XbaI and EcoRI restriction sites to generate the pAAV-EF1a-Cre-WPRE-hGHpolyA construct. The titer of rAAV-retro-EF1a-Cre was 5.0×10^{12} genome copies/mL

as measured by qPCR. The titer of the undiluted RVΔGL-Cre was 4.26×10^{10} infectious units/mL. rAAV2/1-CAG-FLEX-EGFP-WPRE-bGH stock number V5749 with a titer of 1.34×10^{13} genome copies/mL (AAV-FLEX-EGFP) was obtained from the Penn Vector Core.

Viruses were injected into the left hemisphere of adult (P55–134) male and female Ai75 (RCL-nT; Jackson Laboratory #025106) mice using stereotaxic coordinates or intrinsic signal imaging to locate the target region. A total of 7 mice were injected in ACA and 8 in AM, with representative data shown from each animal between Fig. 6 and Supplementary Fig. 5. Stereotaxic coordinates were used for all three tracers in ACA (mm from bregma: AP +0.5, ML –0.25, and DV + 0.9 from brain surface), and for RVΔGL-Cre and AAV-retro-EF1a-Cre injections into area AM (AP –2.18, ML –1.6, DV +0.55). CAV2-Cre injections into AM were guided by sign maps derived from intrinsic signal imaging results for each animal (injection depths 0.3 and 0.6 mm from brain surface with a 20° pipette angle[74]; see also methods in ref. [75].

For paired intersectional injections in mice, AAV-FLEX-EGFP was injected into ACA at (mm from bregma: AP +1.1, ML –0.25, and DV 0.9 and 1.3 from brain surface) using iontophoresis (5 µA, 5 min at each depth) and RVΔGL-Cre was injected into RSP at (mm from bregma: AP –2.06, ML –0.17, and DV 0.8 from brain surface) using pressure injection. The two injections were performed during a single surgical procedure. All retrograde viruses were injected via pressure using a Nanoject II system (CAV2-Cre; 100–200 nL; RVΔGL-Cre 250 nL; rAAV2-retro-EF1a-Cre, 50 nL). Twenty-one days after virus injection, mice were perfused with 4% paraformaldehyde (PFA), then brains were dissected and postfixed in 4% PFA at room temperature (22–25 °C) for 3–6 h, followed by overnight at 4 °C. CAV2-Cre injected brains were stored in PBS with 0.1% sodium azide before proceeding to serial two-photon (STP) imaging using a TissueCyte 1000 system (TissueVision, Inc.) as described[76]. Briefly, coronal images were acquired every 100 µm through the entire rostrocaudal extent of the brain, with *xy* resolution of 0.35 µm/pixel. RVΔGL-Cre and rAAV2-retro-EF1a-Cre injected brains were stored in 10% sucrose in PBS before sectioning at 50-µm intervals with a microtome (Leica SM2000 R). Sections were mounted on gelatin-coated slides and stained for 10 min with 5 µM 4′,6-diamidino-2-phenylindole (DAPI) in PBS, rinsed for 10 min in PBS and coverslipped using Fluoromount-G (SouthernBiotech). Whole-slide scanning was performed with an Olympus VS110 microscope at 4× magnification. Images were cropped, downsampled and dynamic range-adjusted using Adobe PhotoShop CS6.

The number of retrogradely labeled cells per layer was determined by counting the number of tdTomato$^+$ nuclei in each figure panel, except in rows iii and iv (ORBvl and RSP) of Fig. 6, where a 1 × 1 mm ROI was drawn on the image and counting was performed inside the ROI. Layer boundaries were determined by expert visualization of DAPI labeled nuclei, where available, and pia–white matter distance. To estimate the uptake volume of viral injections, we manually drew polygons around the borders of the densely labeled cells on the images for all tissue sections covering the rostrocaudal extent of the injection site. The area of the polygons was measured using ImageJ, and these areas were converted from pixels to microns and then multiplied by the section thickness (100 µm) to estimate the total volume of the injection site. The volume of injection spread did not differ between viruses (mean ± s.d. = CAV2-Cre: $1.4\pm0.5\,mm^3$, RV-ΔGL-Cre: $1.1\pm0.6\,mm^3$, AAV-retro-EF1a-Cre: $0.6\pm0.4\,mm^3$; $P=0.22$) but was dependent on injection site ($1.5\pm0.4\,mm^3$ for ACA, $0.7\pm0.4\,mm^3$ for VISam; $P=0.02$, two-way ANOVA). All injections spanned the entire thickness of the cortex.

Statistics and reproducibility. Analysis of cell counts (Fig. 3) used two-sided paired *t* tests. Analysis of membrane property differences (Fig. 4) used one-way ANOVA, with Neuman–Keuls post hoc tests where appropriate. Analysis of in vivo response properties (Fig. 5) used a two-sample *z*-score proportion test. Analysis of differences between injection uptake volumes (Fig. 6) used two-way ANOVA. All tests for significance used a cutoff of $P=0.05$. No statistical methods were used to determine sample size, but sample sizes for each type of experiment in this study are consistent with previously published work.

Accession codes. Addgene: pRVdG-4Cre, 98034; pRVdG-4GCaMP6f, 98035; pRVdGL-1EGFP, 98036; pRVdGL-4EGFP, 98037; pRVdGL-1Cre, 98038; pRVdGL-4Cre, 98039; and pRVdGL-4Flpo, 98040.

Life Sciences Reporting Summary. Further information on experimental design is available in the Life Sciences Reporting Summary.

Code availability. Code is available from the authors upon request. The CNMF code for modeling in vivo fluorescence time courses can be found at https://github.com/flatironinstitute/CaImAn.

Data availability. All novel plasmids and their complete sequences have been deposited with Addgene (see "Accession codes" section). The data that support the findings of this study are available from the corresponding author upon reasonable request.

References

50. Finke, S. & Conzelmann, K. K. *J. Virol.* **73**, 3818–3825 (1999).
51. Finke, S., Mueller-Waldeck, R. & Conzelmann, K. K. *J. Gen. Virol.* **84**, 1613–1621 (2003).
52. Paterson, R. G., Russell, C. J. & Lamb, R. A. *Virology* **270**, 17–30 (2000).
53. Matsuda, T. & Cepko, C. L. *Proc. Natl. Acad. Sci. USA* **101**, 16–22 (2004).
54. Marr, R. A. et al. *J. Mol. Neurosci.* **22**, 5–11 (2004).
55. Niwa, H., Yamamura, K. & Miyazaki, J. *Gene* **108**, 193–199 (1991).
56. Atasoy, D., Aponte, Y., Su, H. H. & Sternson, S. M. *J. Neurosci.* **28**, 7025–7030 (2008).
57. Shaner, N. C. et al. *Nat. Methods* **5**, 545–551 (2008).
58. Koresawa, Y. et al. *J. Biochem.* **127**, 367–372 (2000).
59. Wickersham, I. R., Sullivan, H. A. & Seung, H. S. *Nat. Protoc.* **5**, 595–606 (2010).
60. Wickersham, I. R. & Sullivan, H. A. *Cold Spring Harb. Protoc.* **2015**, 375–385 (2015).
61. Wickersham, I. R. et al. *Cold Spring Harb. Protoc.* **2015**, 368–374 (2015).
62. Madisen, L. et al. *Nat. Neurosci.* **13**, 133–140 (2010).
63. Madisen, L. et al. *Neuron* **85**, 942–958 (2015).
64. Tallquist, M. D. & Soriano, P. *Genesis* **26**, 113–115 (2000).
65. Mayford, M. et al. *Science* **274**, 1678–1683 (1996).
66. Husson, T. R., Mallik, A. K., Zhang, J. X. & Issa, N. P. *J. Neurosci.* **27**, 8665–8675 (2007).
67. Andermann, M. L., Kerlin, A. M., Roumis, D. K., Glickfeld, L. L. & Reid, R. C. *Neuron* **72**, 1025–1039 (2011).
68. Pologruto, T. A., Sabatini, B. L. & Svoboda, K. *Biomed. Eng. Online* **2**, 13 (2003).
69. Thévenaz, P., Ruttimann, U. E. & Unser, M. *IEEE Trans. Image. Process.* **7**, 27–41 (1998).
70. Peng, H., Bria, A., Zhou, Z., Iannello, G. & Long, F. *Nat. Protoc.* **9**, 1 93–208 (2014).
71. Peirce, J. W. J. *Neurosci. Methods* **162**, 8–13 (2007).
72. Pnevmatikakis, E. A. et al. *Neuron* **89**, 285–299 (2016).
73. Hnasko, T. S. et al. *Proc. Natl. Acad. Sci. USA* **103**, 8858–8863 (2006).
74. Garrett, M. E., Nauhaus, I., Marshel, J. H. & Callaway, E. M. *J. Neurosci.* **34**, 12587–12600 (2014).
75. Allen Institute for Brain Science. *Allen Mouse Brain Connectivity Atlas Overview* http://help.brain-map.org/download/attachments/2818171/Connectivity_Overview.pdf (2017).
76. Oh, S. W. et al. *Nature* **508**, 207–214 (2014).

nature research

Corresponding author(s): Ian Wickersham

Life Sciences Reporting Summary

Nature Research wishes to improve the reproducibility of the work that we publish. This form is intended for publication with all accepted life science papers and provides structure for consistency and transparency in reporting. Every life science submission will use this form; some list items might not apply to an individual manuscript, but all fields must be completed for clarity.

For further information on the points included in this form, see Reporting Life Sciences Research. For further information on Nature Research policies, including our data availability policy, see Authors & Referees and the Editorial Policy Checklist.

Please do not complete any field with "not applicable" or n/a. Refer to the help text for what text to use if an item is not relevant to your study.
For final submission: please carefully check your responses for accuracy; you will not be able to make changes later.

Experimental design

1. Sample size

   Describe how sample size was determined.

   No formal methods were used, but sample sizes for each type of experiment in this study are consistent with previously published work.

2. Data exclusions

   Describe any data exclusions.

   Animal exclusions only affected the longitudinal experiments in this work, and the criteria were animal health/death. Described in the relevant Methods sections, the exclusion criteria were pre-established in our IACUC protocols.

   Data exclusion criteria are described in the relevant Methods sections, as well as figure legends. Briefly, the whole-cell patch-clamp recording criteria are standard: any significant changes in access resistance or holding current were interpreted as signs of poor cell health, and recordings were terminated. The criteria for in vivo functional recordings were established after observing novel pathologies associated with different viruses (including unexpected calcium time courses, as described extensively in the text). Representatives of excluded data are shown (e.g., Fig 5e). No data points from the in vivo structural imaging experiments were excluded.

3. Replication

   Describe the measures taken to verify the reproducibility of the experimental findings.

   The number of times each experiment was repeated is indicated in the text, and all experimental findings were reliably reproduced.

4. Randomization

   Describe how samples/organisms/participants were allocated into experimental groups.

   No randomization was used.

5. Blinding

   Describe whether the investigators were blinded to group allocation during data collection and/or analysis.

   No blinding was used.

Note: all in vivo studies must report how sample size was determined and whether blinding and randomization were used.

6. Statistical parameters

For all figures and tables that use statistical methods, confirm that the following items are present in relevant figure legends (or in the Methods section if additional space is needed).

n/a	Confirmed
☐	☒ The exact sample size (*n*) for each experimental group/condition, given as a discrete number and unit of measurement (animals, litters, cultures, etc.)
☐	☒ A description of how samples were collected, noting whether measurements were taken from distinct samples or whether the same sample was measured repeatedly
☐	☒ A statement indicating how many times each experiment was replicated
☐	☒ The statistical test(s) used and whether they are one- or two-sided *Only common tests should be described solely by name; describe more complex techniques in the Methods section.*
☐	☒ A description of any assumptions or corrections, such as an adjustment for multiple comparisons
☐	☒ Test values indicating whether an effect is present *Provide confidence intervals or give results of significance tests (e.g. P values) as exact values whenever appropriate and with effect sizes noted.*
☐	☒ A clear description of statistics including central tendency (e.g. median, mean) and variation (e.g. standard deviation, interquartile range)
☐	☒ Clearly defined error bars in all relevant figure captions (with explicit mention of central tendency and variation)

See the web collection on statistics for biologists for further resources and guidance.

Software

Policy information about availability of computer code

7. Software

Describe the software used to analyze the data in this study.	Clampfit 10.6.1.1, GraphPad Prism 6, pClamp10, MATLAB R2013b and R2017a, CaImAn (CNMF) in Python 2.7 (https://github.com/flatironinstitute/CaImAn), Vaa3D 3.2, ImageJ 1.5

For manuscripts utilizing custom algorithms or software that are central to the paper but not yet described in the published literature, software must be made available to editors and reviewers upon request. We strongly encourage code deposition in a community repository (e.g. GitHub). *Nature Methods* guidance for providing algorithms and software for publication provides further information on this topic.

Materials and reagents

Policy information about availability of materials

8. Materials availability

Indicate whether there are restrictions on availability of unique materials or if these materials are only available for distribution by a third party.	All plasmids will be made available through Addgene (nonprofit) for distribution to the scientific community at cost.

9. Antibodies

Describe the antibodies used and how they were validated for use in the system under study (i.e. assay and species).	Chicken anti-GFP polyclonal primary antibody (Aves Labs, GFP-1020) and donkey anti-chicken secondary antibody (Jackson Immuno, #703-585-155); validation with positive and negative controls is shown in Figure 1 and described in the legend and methods.

10. Eukaryotic cell lines

a. State the source of each eukaryotic cell line used.	HEK 293T cells were obtained from ATCC (#CRL-11268); BHK-B19G2 cells were described in Wickersham et al., Nature Protocols 2010 Mar;5(3):595-606 and were originally derived from BHK-21 cells obtained from ATCC (#CCL-10).
b. Describe the method of cell line authentication used.	Cell lines were not specifically authenticated.
c. Report whether the cell lines were tested for mycoplasma contamination.	Cell lines were tested for mycoplasma contamination by ATCC but not subsequently..
d. If any of the cell lines used are listed in the database of commonly misidentified cell lines maintained by ICLAC, provide a scientific rationale for their use.	No commonly misidentified cell lines were used.

Animals and human research participants

Policy information about studies involving animals; when reporting animal research, follow the ARRIVE guidelines

11. Description of research animals

Provide all relevant details on animals and/or animal-derived materials used in the study.

All experiments were conducted using the following strains of Mus musculus:
Ai14 (Jackson Laboratory #007908)
Ai65D (Jackson Laboratory #021875)
Meox2-Cre (Jackson Laboratory #003755)
Ai93 (Jackson Laboratory #024103)
Camk2a-tTA (Jackson Laboratory #007004)
Ai75 (Jackson Laboratory #025106)
C57BL/6 mice (Jackson Laboratory #000664)

Policy information about studies involving human research participants

12. Description of human research participants

Describe the covariate-relevant population characteristics of the human research participants.

No human subjects were used.

nature research

Corresponding author(s): Wickersham, Ian

☐ Initial submission ☐ Revised version ☒ Final submission

Flow Cytometry Reporting Summary

Form fields will expand as needed. Please do not leave fields blank.

Data presentation

For all flow cytometry data, confirm that:

☒ 1. The axis labels state the marker and fluorochrome used (e.g. CD4-FITC).

☒ 2. The axis scales are clearly visible. Include numbers along axes only for bottom left plot of group (a 'group' is an analysis of identical markers).

☒ 3. All plots are contour plots with outliers or pseudocolor plots.

☒ 4. A numerical value for number of cells or percentage (with statistics) is provided.

Methodological details

5. Describe the sample preparation.	HEK 293T cells fixed in 1% PFA and resuspended
6. Identify the instrument used for data collection.	BD Biosciences LSR II
7. Describe the software used to collect and analyze the flow cytometry data.	BD FACSDiva
8. Describe the abundance of the relevant cell populations within post-sort fractions.	No sorting was used.
9. Describe the gating strategy used.	No gating was used for sorting because no sorting was used.

Tick this box to confirm that a figure exemplifying the gating strategy is provided in the Supplementary Information. ☐